Applied Water Science (2019) 9:175
https://doi.org/10.1007/s13201-019-1076-8

ORIGINAL ARTICLE

Zirconia nanoparticle-modified graphitic carbon nitride nanosheets for effective photocatalytic degradation of 4-nitrophenol in water

Mohanna Zarei[1] · Jamil Bahrami[1] · Mohammad Zarei[1]

Received: 9 April 2017 / Accepted: 10 October 2019 / Published online: 14 October 2019

Abstract

Zirconia (ZrO_2)-modified graphitic carbon nitride (g-C_3N_4) nanocomposite was used for effective photodegradation of 4-nitrophenol (4-NP) in water. The ZrO_2 nanoparticles, g-C_3N_4 nanosheets, and ZrO_2/g-C_3N_4 nanocomposite were well characterized by including N_2 adsorption, X-ray diffraction, Fourier transform infrared spectroscopy, field emission scanning electron microscopy, UV–Vis diffuse reflectance spectroscopy, photoelectrochemical measurements, and photoluminescence spectroscopy methods. ZrO_2/g-C_3N_4 nanocomposites were formed at room temperature using sonication and used for effective for photodegradation of 4-NP under irradiation with visible light. The nanocomposite samples resulted in a significant increase in photocatalytic activity compared with single-component samples of g-C_3N_4. In particular, the ZrO_2/g-C_3N_4 nanocomposite exhibited the significant increase in the photocatalytic activity. The ZrO_2/g-C_3N_4 nanocomposite showed an excellent catalytic activity toward the reduction of 4-NP in aqueous medium. Further, ZrO_2/g-C_3N_4 nanocomposite can be reused several times for photocatalytic degradation as well as for 4-NP adsorption.

Keywords Graphitic carbon nitride · Zirconia · Photocatalysis · Water purification · Nanostructures

Introduction

Extensive global industrial activities have resulted in severe negative impacts on the environment through air and water pollution and generation of large amounts of waste materials. Industrial waste materials consist of both organic and inorganic substances such as pesticide residues, chlorinated and volatile compounds, nitro aromatics, detergents, chemical dyes, and fertilizers. Among the various toxic wastes, dyes and nitro aromatic compounds caused the greatest concern due to their high chemical and biological stability. The US Environmental Protection Agency has declared 4-NP a hazardous pollutant (Atlow et al. 1984; Klibanov et al. 1983). 4-NP can disturb functioning of the human central network system and cause damage to kidneys and the liver (Pohanish 2008; Zarei et al. 2016). Thus, removal of 4-NP from polluted water is essential. Traditional water remediation treatments are not effective for the removal of 4-NP due to its stability and solubility in water. Therefore, recently, the scientific community has given focused on inventing efficient catalysts for the degradation of 4-NP (Chang et al. 2012; Pradhan et al. 2002).

Semiconductor photocatalysis is the emerging advanced oxidation method for abatement of organic pollutants and possesses several advantages over traditional oxidation methods. One of the merits of semiconductor photocatalysis is the ability of adsorbing a wide range of organic and inorganic species on the surface of the photocatalyst which chemically alters by light-induced redox reaction. Various types of photocatalysts for use in air or water purification applications have been designed (Pawar et al. 2015). Combinations of metal/metal oxide nanoparticles (NPs) such as Au, Ag, Pt, TiO_2, ZnO, SnO_2, WO_3, Nb_2O_5, $BiVO_4$, and Fe_2O_3 with conducting polymers such as polyaniline, polypyrrole, and polythiophene have been utilized for the degradation of organic pollutants (Ge et al. 2013; Jiang et al. 2014; Reimer et al. 2014; Wang and Astruc 2014; Wang et al. 2014; Xu et al. 2014; Zhang et al. 2015b). The small dimensions induce a significant change in the reduction potential of

✉ Mohammad Zarei
Mo.zarei@alumni.um.ac.ir

Mohanna Zarei
mohannazarei@eng.uok.ac.ir

Jamil Bahrami
jbahrami@uok.ac.ir

[1] Department of Civil Engineering, University of Kurdistan, Sanandaj 66177-15175, Iran

metal NPs compared to bulk materials. This unique characteristic improves the electron transfer process in various catalysis reactions. However aggregation, agglomeration, and high surface energy of NPs reduce the feasibility of NP applications as photocatalysts. In order to reduce aggregation, NPs can be stabilized on the surface of a solid support (Campelo et al. 2009). Carbonaceous nanomaterials are interesting candidates due to their exotic physical and chemical characteristics (Geim 2009) such as high surface area, high electrical-thermal conductivity, high charge carrier mobility, and extraordinary mechanical strength, and graphene allotropes are a promising material for support of different NPs. The graphene support which contains metal or semiconductor NPs has been confirmed to be effective nanocomposite material for the photovoltaic cell (Ong et al. 2015a; Yeh et al. 2015), catalysis, and biosensor applications (Guo and Dong 2011). Recently, another two-dimensional carbonaceous material, g-C_3N_4, has attracted significant attention (Gao et al. 2014; Maeda et al. 2014; Tan et al. 2015; Tian et al. 2014; Wang et al. 2012; Wu et al. 2014; Zheng et al. 2012). Unique properties of g-C_3N_4 including good visible-light absorption, moderate band gap (2.7 eV), high thermal and chemical stability, and photocatalytic properties introduce a new material for application in photocatalysis (Pawar et al. 2016a, 2017). The g-C_3N_4 and g-C_3N_4-based structures have been used in various applications such as photo catalytic degradation of microbial, organic, and inorganic pollutants (Lan et al. 2015; Li et al. 2015; Papailias et al. 2015; Pawar et al. 2015, 2016b), hydrogen evolution from water splitting (Liang et al. 2015; Liu et al. 2015b; Xu et al. 2015; Yang et al. 2015b), sensors applications (Pany and Parida 2015; Wang et al. 2015; Zhang et al. 2015a), adsorption (Anbia and Haqshenas 2015; Chen et al. 2015; Hu et al. 2015), reduction of oxygen (Lu et al. 2015; Zhao et al. 2015), lithium-ion batteries (Liu et al. 2015a; Luo et al. 2015), biofuel cells (Yi et al. 2015), and photochemo combination methods (Yang et al. 2015a). Due to repeating triazine units, the g-C_3N_4 consists of a large number of binding sites which can stabilize the NPs, making this g-C_3N_4 a promising support for NPs (Huang et al. 2015; Ong et al. 2015b). Thus, g-C_3N_4 nanosheet can be used as a feasible candidate for stabilizing metal NPs for catalytic applications (Wang et al. 2009). This material is used for the degradation of organic pollutants and photocatalytic reduction of CO_2 under visible light (Mao et al. 2013; Yan et al. 2009). However, it suffers from a high charge carrier recombination rate and low quantum efficiency which lead to poor photocatalytic performance (Wang et al. 2012). Sensitization and combination with semiconductor NPs (namely Au, Ag, Pt, and Pd) and carbon-based materials (CNTs and graphene) are the most viable routes for improving the g-C_3N_4-based photocatalysts (Sridharan et al. 2014). Among the metal oxide NPs, ZrO_2 is a material with favored properties including high stability, high toughness, high chemical strength, desirable corrosion, chemical and microbial resistance (Polisetti et al. 2011; Singh and Nakate 2014). Moreover, ZrO_2 NPs have plenty of oxygen vacancies on surfaces with wideband-gap P-type semiconductors. The high ion exchange ability and redox movement make it useful in many catalytic processes as a catalyst (Fidelus et al. 2012).

Here, we report a facile ultrasonication method for the fabrication of hybrid nanocomposites using ZrO_2 NPs, and g-C_3N_4 nanosheets and their application for photocatalytic degradation of 4-NP in water. Mono-dispersed ZrO_2 NPs were dispersed on carbon nitride sheets by ultrasound. The ZrO_2/g-C_3N_4 composite exhibited superior catalytic activity toward the reduction of 4-NP. Possible mechanism for degradation of 4-NP upon ZrO_2/g-C_3N_4 catalyst under light irradiation was proposed. The ZrO_2/g-C_3N_4 catalyst is very efficient for the removal of 4-NP from aqueous environment by its dual actions with adsorption and photocatalytic degradation of 4-NP.

Materials and methods

Materials

All reagents were of analytical grade. Hydrochloric acid and ammonia were purchased from Merck. $ZrOCl_2{\cdot}8H_2O$, KOH, and nitric acid were purchased from Sigma-Aldrich. Melamine (99%) was prepared from Sigma-Aldrich and used without further purification. P25 titanium dioxide (TiO_2) powder was obtained from Degussa (rutile/anatase: 85:15, 99.9%).

Synthesis of ZrO_2 NPs

In a typical synthesis, 0.1 M of $ZrOCl_2{\cdot}8H_2O$ was dissolved in 100 mL of distilled water. Then, 0.3 M of KOH was added to the above solution. The final solution was transferred into a stainless steel Teflon-lined sterilized capacity of 100 mL and kept in an oven at 180 °C for 16 h. The resulting precipitates were washed with distilled water and ethanol. The resultant was dried for 3 h in vacuum at 80 °C.

Synthesis of g-C_3N_4 nanosheets

In a typical synthesis, 30 g melamine was placed in a crucible and then heated at 600 °C for 2 h, resulting in yellow powder. Liquid exfoliating method was applied to produce the g-C_3N_4 nanosheets from bulk material. In brief, 70 mg of the bulk g-C_3N_4 powder was dispersed in 100 mL water and the mixture was ultrasounded for 6 h. The final suspension was then centrifuged at 10,000 rpm and dried for 3 h in vacuum at 80 °C (Tian et al. 2013).

Fabrication of ZrO_2/g-C_3N_4 hybrids

The ZrO_2 NPs was incorporated into g-C_3N_4 sheets using ultrasonication at room temperature. Then, 50 mg of g-C_3N_4 powder was added to 20 mL of the ZrO_2 colloidal dispersion and ultrasonicated for 2 h at 30 °C. The ZrO_2/g-C_3N_4 dispersion was then filtered and washed several times using ethanol. The resulting ZrO_2/g-C_3N_4 powder was collected and dried overnight at 60 °C.

Characterization methods

The X-ray diffraction (XRD) pattern of the nanomaterials was obtained by using a powder X-ray diffractometer model Shimadzu XRD 6000 using CuKa with a diffraction angle between 20° and 80°. The crystallite size was determined using Scherrer's formula. Field emission Scanning electron microscopy (FESEM) studies were carried out on TSCAN. UV–Vis absorption spectrum for the samples was recorded using a Varian spectrophotometer in the range of 300–700 nm. The Fourier transform infrared spectroscopy (FTIR) spectrum of the ZrO_2 NPs was taken using an FTIR model THERMO NICOLET Spectrometer. The photoluminescence (PL) spectrum of the ZrO_2 particles was recorded by the PerkinElmer lambda spectrophotometer with a Xenon lamp as the excitation light source.

Photocatalytic degradation

The photocatalytic activities of ZrO_2/g-C_3N_4 hybrids were evaluated at room temperature. Thirty–sixty milligrams of sample was dispersed into the 100 mL of 30 mg/L 4-NP solution with magnetic stirring in each experiment. Prior to irradiation, the suspensions were magnetically stirred in the dark for 60 min to reach an adsorption/desorption equilibrium between the catalyst and 4-NP solution. Then, the solution was exposed to simulated solar light under magnetic stirring. At given reaction time of approximately 2 h, 4 mL of the solution was pipetted every 10 min and centrifuged to separate the catalyst. Concentration of 4-NP solution was measured by a UV–visible spectrophotometer at $\lambda = 500$ nm to evaluate the degradation rate. The examination experiment of reactive species is similar to the photodegradation experiment. The catalytic degradation efficiency of 4-NP was calculated using Eq. (1):

$$\%\ \text{Degradation Efficiency} = \frac{C_0 - C_e}{C_0} 100 \quad (1)$$

where C_0 is initial concentration of 4-NP solution (mg L^{-1}) and C_e is the equilibrium concentration of 4-NP solution (mg L^{-1}).

Photoelectrochemical measurements

Photoelectrochemical (PEC) performance was analyzed using a three-electrode in quartz cell. Graphite served as the counter electrode, and Ag/AgCl served as the reference. The PEC measurements were taken using a Xe arc lamp (300 W, model 66984; Oriel, USA) with the electrolyte solution of Na_2SO_4 (0.5 M). For preparation of working electrodes, 10 mg of g-C_3N_4 powder was added to 10 mL of Liquion solution, and the resulted mixture was ultrasonicated for 1 h and stirred overnight. This suspension was spin-coated on a fluorine-doped tin oxide (FTO) glass substrate at ambient conditions. At final stage, in order to increase the uniform distribution of the catalyst on the substrate, the prepared FTO films spin-coated with the catalysts were heated in oven at 60 °C for 2 h (Pawar et al. 2016a).

Results and discussion

Characterizations of ZrO_2/g-C_3N_4 composites

Figure 1a–c shows the XRD patterns of the g-C_3N_4, ZrO_2, and ZrO_2/g-C_3N_4 nanocomposites. The diffraction peaks of ZrO_2 NPs can be assigned to the monoclinic phase. ZrO_2 NPs are spherical with an average particle size of 15 nm, which leads to its high surface area of 73.9 $m^2\ g^{-1}$. However, pure g-C_3N_4 has a low surface area of 51.8 $m^2\ g^{-1}$, which can be attributed to its special morphology. The BET surface area analysis applied using the N_2 adsorption method illustrates that the incorporation of ZrO_2 NPs increases the surface area of g-C_3N_4 nanosheets. The BET surface area of 10 wt% ZrO_2/g-C_3N_4 and 30 wt% ZrO_2/g-C_3N_4 samples was 59.12 and 65.3 $m^2\ g^{-1}$, respectively. The BET surface areas result shows that the addition of ZrO_2 increases the surface area of g-C_3N_4. The strong and sharp ZrO_2 diffraction peaks demonstrate that the samples have high crystallinity. The XRD patterns show no extra diffraction peaks indicating the high level of purity of the samples. Diffraction peaks of g-C_3N_4 at 12.8° and 27.6 ° confirmed that g-C_3N_4 was formed. The XRD patterns of ZrO_2/g-C_3N_4 hybrid samples contain the peaks of both ZrO_2 NPs and g-C_3N_4 nanosheets and show that after synthesis of ZrO_2/g-C_3N_4 composite, the crystal structure of ZrO_2 and g-C_3N_4 did not change. Figure 1d–f illustrates field emission scanning emission microscopy (FESEM) images of the ZrO_2, g-C_3N_4, and ZrO_2/g-C_3N_4 hybrid samples which show the planar structure of g-C_3N_4 nanosheets as well as the spherical structure of ZrO_2 NPs.

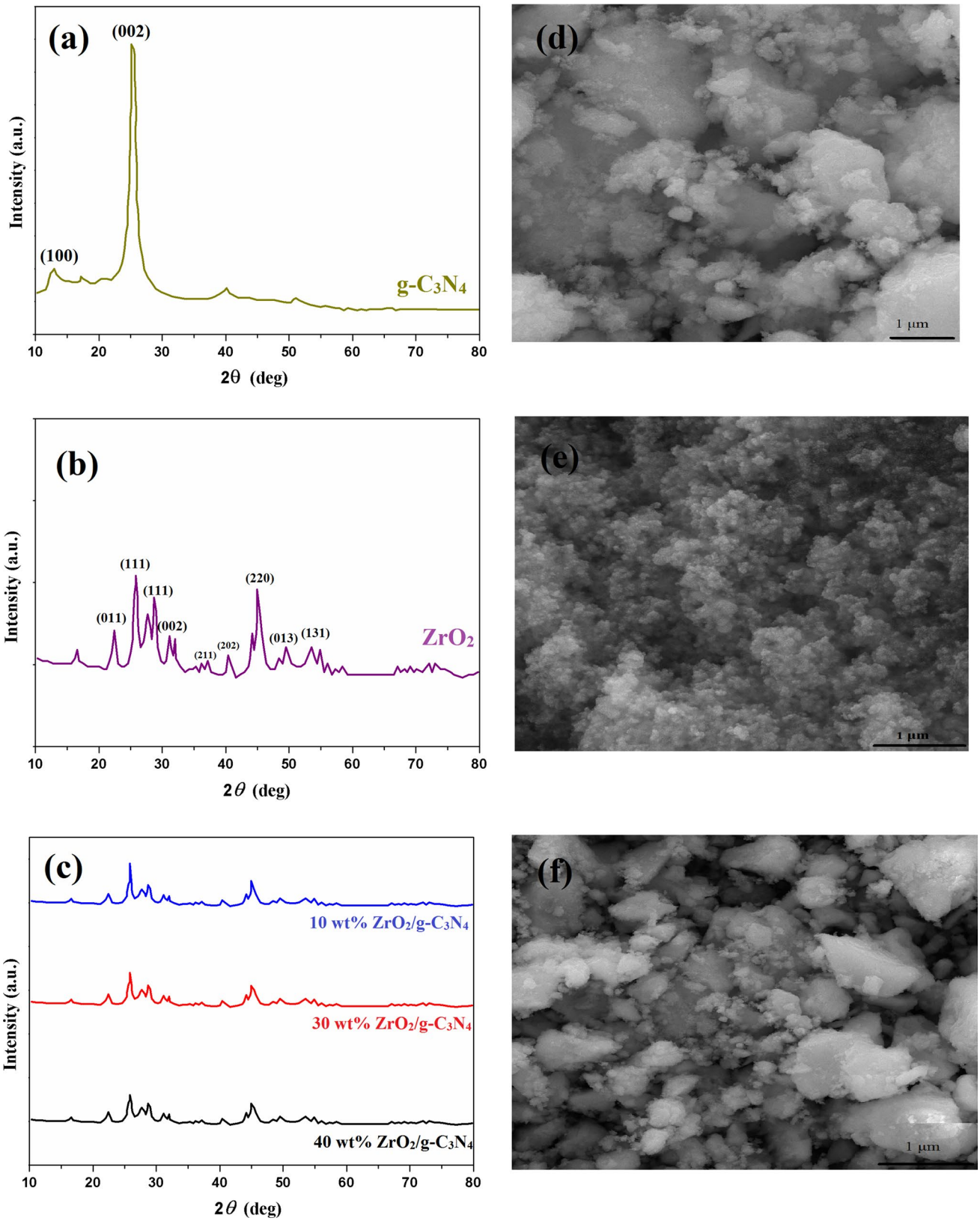

Fig. 1 XRD patterns of **a** g-C_3N_4, **b** ZrO_2 and **c** ZrO_2/g-C_3N_4 composites with different ZrO_2 concentrations. FESEM images of **d** g-C_3N_4, **e** ZrO_2, and **f** 20.9 wt% ZrO_2/g-C_3N_4 composite (**e** and **f**). (green color: g-C_3N_4, violet color: ZrO_2, blue color: 10 wt% ZrO_2/g-C_3N_4, red color: 30 wt% ZrO_2/g-C_3N_4, block color: 40 wt% ZrO_2/g-C_3N_4)

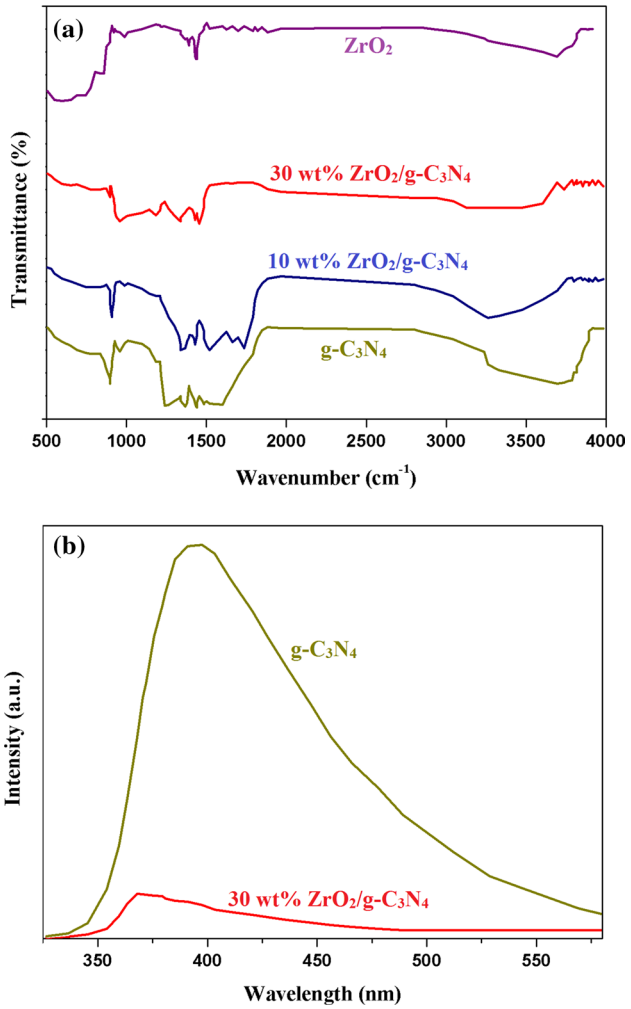

Fig. 2 **a** FTIR spectra of ZrO_2/g-C_3N_4 composites with different ZrO_2 concentrations, **b** PL spectra of g-C_3N_4 and 30 wt% ZrO_2/g-C_3N_4

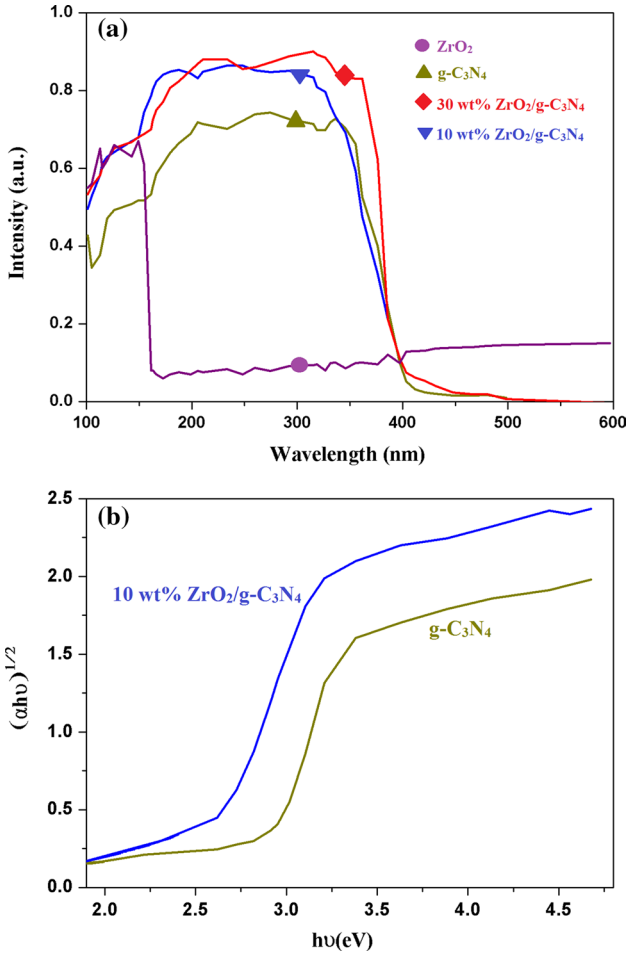

Fig. 3 **a** UV–Vis diffuse reflectance spectra (DRS) of pure g-C3N4, ZrO_2, 10 wt% ZrO_2/g-C_3N_4, 30 wt% ZrO_2/g-C_3N_4 and **b** the optical absorption edges of the representative 10 wt% ZrO_2/g-C_3N_4 and pure g-C_3N_4

Figure 2a shows the FTIR spectra for ZrO_2, g-C_3N_4, and ZrO_2/g-C_3N_4 nanocomposites. For ZrO_2, the broad bands at the range 500–550 cm^{-1} and 800 cm^{-1} are related to the Zr–O vibration absorption (Zhang et al. 2013). Furthermore, the broad region with a maximum of about 3350 cm^{-1} can be related to the hydroxyl groups of hydrated oxide. For g-C_3N_4, the sharp peaks in the range of 1200–1700 cm^{-1} can be attributed to the stretching vibration of the breathing mode of triazine units (Sayama and Arakawa 1993). In addition, a broad absorption band with a maximum of around 3200–3700 cm^{-1} can be attributed to the N–H groups (Sayama and Arakawa 1993). There is a similarity between the FTIR spectra of ZrO_2/g-C_3N_4 and pure g-C_3N_4. However, the change in the bands of 800 and 3300 cm^{-1} with the variation of ZrO_2 concentration still demonstrates the presence of ZrO_2 NPs. The FTIR result shows good correlation with XRD results and shows the hybrids structure of ZrO_2/g-C_3N_4 nanocomposite (Sayama and Arakawa 1993).

Figure 2b shows the influence of the ZrO_2/g-C_3N_4 hetero-junction on the separation efficiency of electron–hole pairs which was investigated by PL spectra. Sharp emission peak at around 380 nm in unmodified g-C_3N_4 related to the band gap transition emission which is equal to the band gap energy of unmodified g-C_3N_4. However, fluorescence quenching can be observed in the similar position in the PL spectrum of ZrO_2/g-C_3N_4. Further, charge transfer between g-C_3N_4 and ZrO_2 component prevents the electron–hole recombination.

Compared with that of g-C_3N_4, the emission intensities of ZrO_2/g-C_3N_4 are much lower, which indicate that a good separation of electrons and holes is achieved by introducing ZrO_2 NPs to the g-C_3N_4 nanosheets.

The ability to absorb the light by photocatalysts is important to generate the charge carriers. Therefore, we measured the optical characteristics in g-C_3N_4, ZrO_2, and ZrO_2/g-C_3N_4 nanocomposites using the UV–Vis diffuse reflectance

spectroscopy (DRS) technique. As shown in Fig. 3a, ZrO_2 NPs absorbed the light with a wavelength shorter than 170 nm have band gap energy of about 4.8 eV. In pure g-C_3N_4, the absorbance edge is located at 415 nm, revealing the standard absorption threshold of g-C_3N_4 structure (Wang et al. 2009; Yan et al. 2009). Because of interactions between ZrO_2 and g-C_3N_4, the ZrO_2/g-C_3N_4 nanocomposite (10, 30 wt% ZrO_2/g-C_3N_4) shows better photo absorption performance than pure g-C_3N_4. Different chemical bonds formed between the ZrO_2 and g-C_3N_4 might result in the enhanced optical property which is similar to that in the N-doped ZrO_2 (Zhao et al. 2014) and TiO_2-doped graphene photocatalyst (Leary and Westwood 2011; Woan et al. 2009). According to DRS results, ZrO_2/g-C_3N_4 nanocomposite shows an efficient visible-light photocatalytic activity. When ZrO_2 was incorporated into g-C_3N_4 nanosheets, the corresponding band edge absorption was shifted to longer wavelength in comparison with the pure g-C_3N_4. The nanocomposite structures of 30 wt% ZrO_2/g-C_3N_4 exhibited maximum absorption in the visible region of spectrum. Moreover, we estimated band gap energy of pure g-C_3N_4 and ZrO_2/g-C_3N_4 nanocomposite from optical absorption, and the corresponding plots are shown in Fig. 3b. The direct band gap of pure ZrO_2 is calculated to be 5.20 eV, which is seen to be not useful in visible region of solar spectrum. However, after making nanocomposite with g-C_3N_4, it shifted toward visible region. The obtained band gap of pure g-C_3N_4 is found to be 2.75 eV, which can be used in visible irradiation. Additionally, nanocomposite structure exhibited band edge absorption around 2.6 eV, indicating its applicability in visible light. Figure 3a shows the UV–Vis spectra of all the ZrO_2 samples have extended a red shift and significant absorption between 100 and 450 nm. This red shift translates into a decrease in the band gaps of the nanocomposites which leads to more absorption in the visible region and hence better photocatalytic activity. In general, the red shift and absorption intensity both increased with higher ZrO_2 concentration. In addition, the optical spectra of the ZrO_2/g-C_3N_4 display clear red shifts with respect to that of pure g-C_3N_4 which is consistent with the band gaps calculated from the DRS results. The enhanced visible-light absorption of ZrO_2/g-C_3N_4 materials makes them ideal candidates for photocatalysts. Hence, the band gap value of the nanocomposite decreases by increasing the amount of g-C_3N_4. This result indicated the strong interaction between ZrO_2 and g-C_3N_4 nanosheets in the nanocomposite.

Photocatalytic degradation of 4-NP

Figure 4 shows the degradation of 4-NP under visible-light irradiation for determination of photocatalytic activity of ZrO_2, g-C_3N_4, and ZrO_2/g-C_3N_4 nanocomposites. For comparison, the degradation of 4-NP by TiO_2 powder was

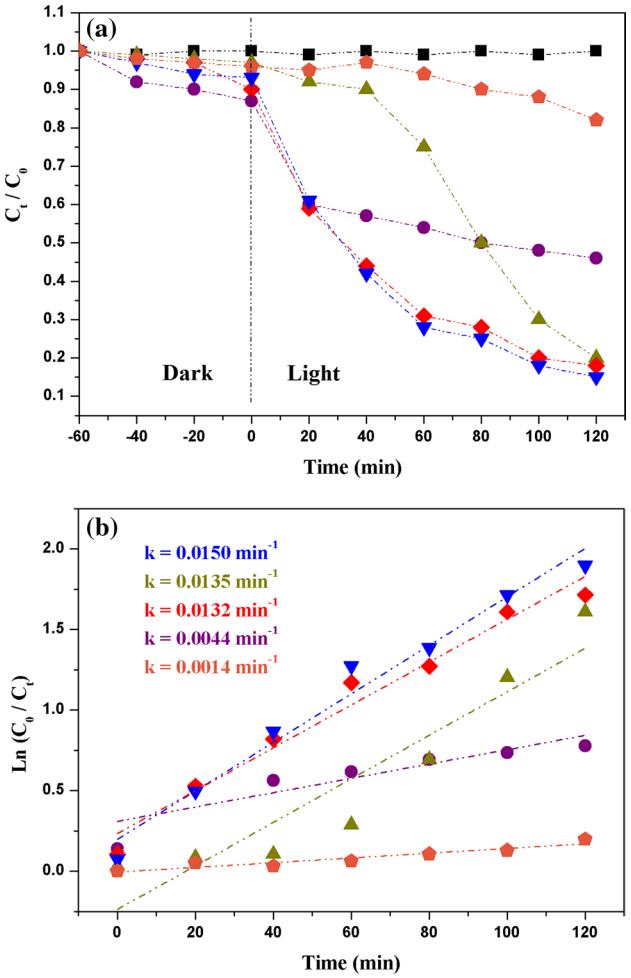

Fig. 4 **a** Photodegradation of 4-NP on ZrO_2/g-C_3N_4 nanocomposites under light irradiation and **b** the corresponding reactive constant (green color triangle: g-C_3N_4, violet color circle: ZrO_2, red color diamond: 10 wt% ZrO_2/g-C_3N_4, blue color down triangle: 30 wt% ZrO_2/g-C_3N_4, brown color pentagon: TiO_2, block color square: blank)

analyzed as a standard material. The blank test shows that 4-NP is stable under visible-light irradiation, which indicates that the contribution of 4-NP photolysis can be neglected. Also, ZrO_2 NP has a high surface area and demonstrated the stable adsorption for 4-NP. Elevated 4-NP concentration at the beginning of the light-on was attributed to desorption of some 4-NPs due to the increased temperature on the ZrO_2 surface. In irradiation time longer than 30 min, the concentration of 4-NP gradually decreases.

Compared to ZrO_2, pure g-C_3N_4 shows weaker adsorption of 4-NP but higher photoactivity under visible-light irradiation. The rate of 4-NP degradation is 0.0116 min^{-1} which is higher than that of ZrO_2 (0.0022 min^{-1}). The incorporation of ZrO_2 NPs on g-C_3N_4 nanosheets can improve the electron–hole separation efficiency and also in absorption of light. Thus, the catalytic activity for 4-NP degradation is enhanced. By loading of ZrO_2 NPs with

concentration from 10 to 30 wt%, the photocatalytic activity of ZrO_2/g-C_3N_4 increases. According to the results, the 30 wt% ZrO_2/g-C_3N_4 sample demonstrates the highest degradation rate of 0.0167 min^{-1} which is higher than that of pure g-C_3N_4 nanosheets. Also, the prepared ZrO_2/g-C_3N_4 exhibited higher catalytic activity and degradation rate than TiO_2 powder.

Figure 5 shows the photocatalytic activity of 30 wt% ZrO_2/g-C_3N_4 with different scavengers (2-propanol (IPA), $KBrO_3$, benzoquinone (BQ), KI, and NaF). From Fig. 5, it can be observed that IPA which is ·OH scavenger (He et al. 2013; Li et al. 2009) showed little impact on the reaction rate (k) of 4-NP degradation. Although, the addition of BQ, which is $\cdot O^{-2}$ scavenger (Cui et al. 2013; Yang et al. 2013), decreased the k from 0.0317 to 0.0063 min^{-1}. The k also had a clear drop to 0.0078 min^{-1} in the existence of KI (h^+ and ·OH scavenger) (He et al. 2013; Li et al. 2009). This result demonstrates the role of h^+ and $\cdot O^{-2}$ in the photocatalytic degradation of 4-NP on ZrO_2/g-C_3N_4 nanocomposites.

Photoelectrochemical measurement

Transient photocurrent response was measured to investigate the separation efficiency of photogenerated electrons and holes pairs of the ZrO_2 NPs, g-C_3N_4 nanosheets, ZrO_2/g-C_3N_4 nanocomposite. As shown in Fig. 6a, ZrO_2, g-C_3N_4, and ZrO_2/g-C_3N_4 samples demonstrated good reproducibility and stability under several on–off cycles of light illumination. However, the ZrO_2/g-C_3N_4 exhibited stronger and higher photocurrent than ZrO_2 and g-C_3N_4. The reason for this response in hybrid sample related to the existence of numerous charge carriers which enhances the photocatalytic

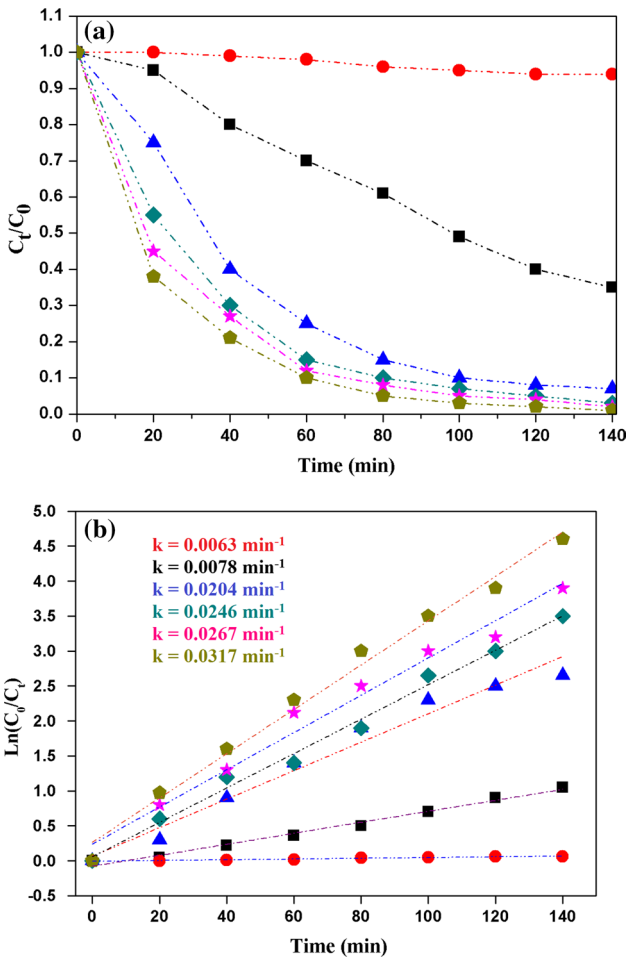

Fig. 5 Effects of scavengers on the photodegradation of 4-NP by ZrO_2/g-C_3N_4 (red color circle: BQ, block color square: KI, pink color star: IPA, light green color diamond: NaF, blue color triangle: $KBrO_3$, dark green color pentagon: no scavenger)

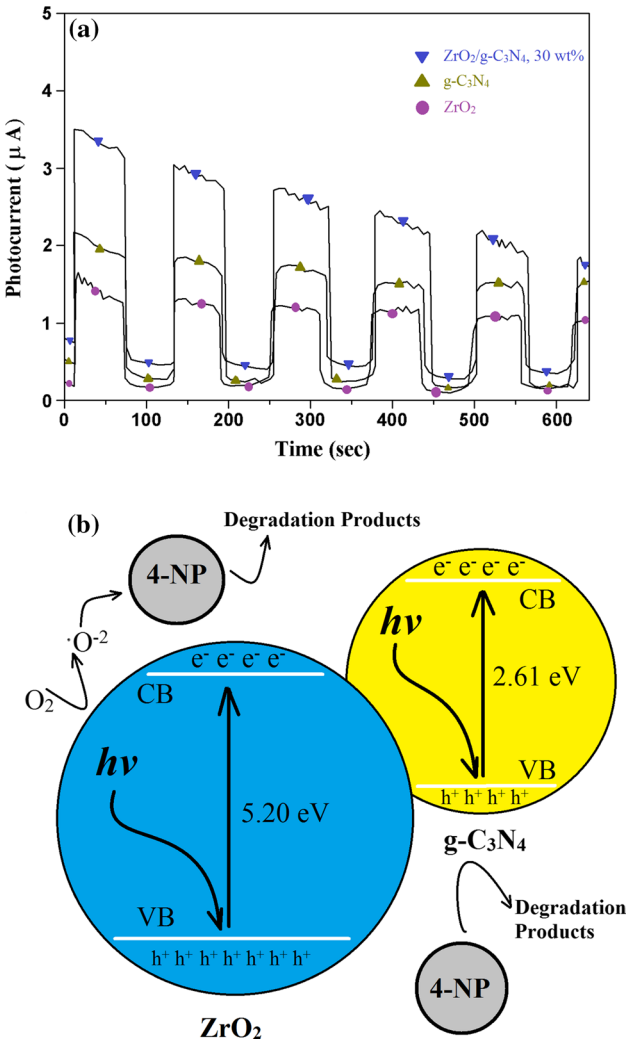

Fig. 6 **a** Transient photocurrent responses of pure ZrO_2, g-C_3N_4, and ZrO_2/g-C_3N_4 nanocomposites under visible-light irradiation, **b** schematic of electron–hole pairs separation and the possible reaction mechanism on ZrO_2/g-C_3N_4 nanocomposite under light irradiation

activity. Furthermore, it confirms the strong interaction of ZrO_2 NPs and g-C_3N_4 nanosheets in hybrid sample.

Photocatalytic mechanism

Incorporation of ZrO_2 NPs on g-C_3N_4 nanosheets generates an efficient photocatalyst for degradation of 4-NP under visible-light irradiation. The addition of ZrO_2 NPs can enhance the surface area and light absorption capacity of g-C_3N_4 nanosheets. In general, two possible reaction mechanisms should be considered for the 4-NP degradation: (a) photolysis and (b) photocatalytic process. In photolysis, energy could be transferred from 4-NP to O_2 to produce an oxygen atom (O) which can oxidize 4-NP as follows:

$$\text{4-NP} + h\nu \rightarrow \text{4-NP}^* \tag{2}$$

$$\text{4-NP}^* + O_2 \rightarrow \text{4-NP} + 2O \tag{3}$$

$$\text{4-NP} + O \rightarrow \text{Degradation products.} \tag{4}$$

Figure 4a shows no 4-NP degradation in the blank experiment under visible light, which confirms that the 4-NP is stable and the photolysis has a negligible contribution in the degradation of 4-NP. In the photocatalytic degradation by NPs, it can be described that the promotion of an electron from the valence band (VB) to the conduction band (CB) by light irradiation generates the active site (hole) for the oxidation of the 4-NP. According to the band gap structure of ZrO_2/g-C_3N_4 and the influence and role of scavengers, possible pathway of the photocatalytic reaction with ZrO_2/g-C_3N_4 was proposed (Eqs. 5–9). The schematic diagram of 4-NP degradation on ZrO_2/g-C_3N_4 is illustrated in Fig. 6:

$$ZrO_2/\text{g-}C_3N_4 + h\nu \rightarrow ZrO_2/\text{g-}C_3N_4\left(e^- + h^+\right) \tag{5}$$

$$ZrO_2/\text{g-}C_3N_4\left(e^- + h^+\right) + h\nu \rightarrow ZrO_2(e^-)/\text{g-}C_3N_4\left(h^+\right) \tag{6}$$

$$ZrO_2(e^-) + O_2 \rightarrow \cdot O_2^- \tag{7}$$

$$\cdot O_2^- + \text{4-NP} \rightarrow \text{Degradation products} \tag{8}$$

$$\text{g-}C_3N_4\left(h^+\right) + \text{4-NP} \rightarrow \text{Degradation products.} \tag{9}$$

Separation efficiency of electron–hole pairs plays an important role in photocatalytic degradation of 4-NP. Electrons of ZrO_2 NPs and g-C_3N_4 were excited from VB to CB which generated the holes in the VB for both semiconductors under the light irradiation. The CB of g-C_3N_4 nanosheet is more negative than that of O_2 molecules (Song and Zhang 2008) which led to excitation of the electrons and diffusion to the g-C_3N_4 surface followed by reaction with oxygen molecules and generation of $\cdot O^{-2}$ radicals. The highly reactive $\cdot O^{-2}$ radicals have high oxidation capability and can degrade the 4-NP molecules on photocatalyst surface. Further, the CB of g-C_3N_4 is more negative than that of ZrO_2 and electrons on g-C_3N_4 can directly move to the CB of ZrO_2 NPs. Also, the VB of ZrO_2 is more positive than the VB of g-C_3N_4 and the holes on the VB of ZrO_2 can directly move to the VB of g-C_3N_4. This process can effectively enhance the separation of electron–hole pairs and greatly decrease the charge recombination, resulting in the high photoactivity of ZrO_2/g-C_3N_4 nanocomposites. The VB of ZrO_2/g-C_3N_4 nanocomposites was evaluated according to the concepts of electronegativity. The VB of a semiconductor can be calculated by following equation (Zhang et al. 2009):

$$E_{VB} = X - E^c + 0.5E_g \tag{10}$$

where E_{VB} is the VB potential, E^c is the energy of free electrons (about 4.5 eV), and X is the electronegativity of the semiconductor. The value of X for ZrO_2 is 5.92 eV (Jiang et al. 2010), and the E_{VB} for ZrO_2 was calculated to be 4.11 eV. The conduction band edge potential, E_{CB}, is calculated by:

$$E_{CB} = E_{VB} - E_g. \tag{11}$$

The band gap of the ZrO_2 NPs is about 5.20 eV. The values of E_{VB} and E_{CB} for g-C_3N_4 were reported as 1.53 and − 1.01 eV, respectively (Yan et al. 2010).

Efficiency of the catalyst

To study the efficiency and stability of ZrO_2/g-C_3N_4 nanocomposite, the photocatalytic degradation was repeated by a five-run cycling test under the same condition (Fig. 7). For each run, the photocatalyst was recycled, cleaned, and dried. In each cycle, the suspension was magnetically stirred for 2 h in the presence of light irradiation. The photodegradation of 4-NP was completed in each cycle. Hence, it is plausible

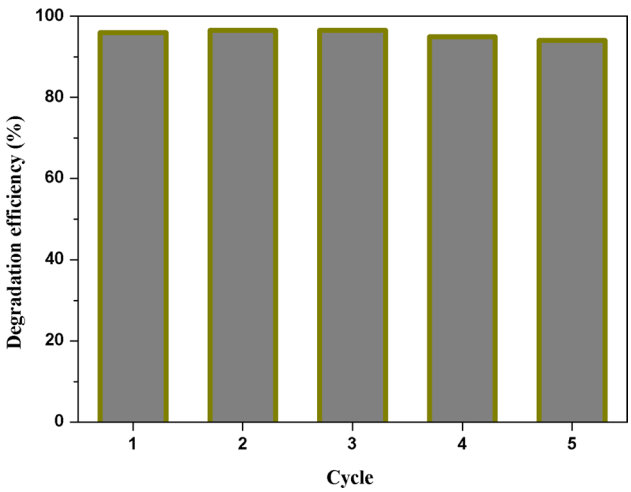

Fig. 7 Reusability of the 30 wt% ZrO_2/g-C_3N_4 photocatalyst in successive cycles

to say that there is no significant loss of catalytic activity even after five cycles.

Conclusions

Nanotechnology-based photocatalysis plays an important role in the future of environmental decontamination, water remediation, and renewable energy generation from water splitting. In this work, ZrO_2/g-C_3N_4 composites were successfully synthesized via simple ultrasound method. The prepared ZrO_2/g-C_3N_4 catalysts were used for photocatalytic degradation of 4-NP. ZrO_2/g-C_3N_4 exhibited higher photocatalytic activity than pure g-C_3N_4 for the degradation of 4-NP under light irradiation, and the 30 wt% ZrO_2/g-C_3N_4 sample showed the highest activity. The XRD, nitrogen sorption, and FESEM results revealed that the ZrO_2/g-C_3N_4 catalysts have high specific surface area. The ZrO_2/g-C_3N_4 nanocomposite is not only a good adsorbent but also a very efficient heterogeneous photocatalyst for the degradation of 4-NP. Moreover, this ZrO_2/g-C_3N_4 nanocomposite can be reused several times for photocatalytic degradation as well as for 4-NP adsorption. Thus, this ZrO_2/g-C_3N_4 composite is a suitable catalyst for water cleaning. It has been shown the ZrO_2 NPs and g-C_3N_4 nanosheets have unique properties such as antibacterial and antimicrobial behavior, environmental friendliness, and non-toxicity (Bing et al. 2015; Gowri et al. 2014). In fact, these characteristics besides the photocatalytic behaviors of g-C_3N_4 and ZrO_2 NPs present a great potential for application of ZrO_2/g-C_3N_4 composite for water remediation purposes.

Acknowledgements The authors acknowledge University of Kurdistan for supporting this project.

References

Anbia M, Haqshenas M (2015) Adsorption studies of Pb(II) and Cu(II) ions on mesoporous carbon nitride functionalized with melamine-based dendrimer amine. Int J Environ Sci Technol 12:2649–2664

Atlow SC, Bonadonna-Aparo L, Klibanov AM (1984) Dephenolization of industrial wastewaters catalyzed by polyphenol oxidase. Biotechnol Bioeng 26:599–603

Bing W, Chen Z, Sun H, Shi P, Gao N, Ren J, Qu X (2015) Visible-light-driven enhanced antibacterial and biofilm elimination activity of graphitic carbon nitride by embedded Ag nanoparticles. Nano Res 8:1648–1658

Campelo JM, Luna D, Luque R, Marinas JM, Romero AA (2009) Sustainable preparation of supported metal nanoparticles and their applications in catalysis. Chemsuschem 2:18–45

Chang G, Luo Y, Lu W, Qin X, Asiri AM, Al-Youbi AO, Sun X (2012) Ag nanoparticles decorated polyaniline nanofibers: synthesis, characterization, and applications toward catalytic reduction of 4-nitrophenol and electrochemical detection of H_2O_2 and glucose. Catal Sci Technol 2:800–806

Chen Q, Zhao Y, Huang X, Chen N, Qu L (2015) Three-dimensional graphitic carbon nitride functionalized graphene-based high-performance supercapacitors. J Mater Chem A 3:6761–6766

Cui H et al (2013) Facile synthesis of graphene oxide-enwrapped Ag_3PO_4 composites with highly efficient visible light photocatalytic performance. Mater Lett 93:28–31

Fidelus JD, Karbowski A, Mariazzi S, Werner-Malento E, Brusa RS, Zhou W, Karwasz GP (2012) Combined positron-annihilation and structural studies of hydrothermally grown zirconia. Nanomater Energy 1:97–105

Gao H, Yan S, Wang J, Zou Z (2014) Ion coordination significantly enhances the photocatalytic activity of graphitic-phase carbon nitride. Dalton Trans 43:8178–8183

Ge L, Han C, Xiao X, Guo L (2013) Synthesis and characterization of composite visible light active photocatalysts MoS_2–gC_3N_4 with enhanced hydrogen evolution activity. Int J Hydrog Energy 38:6960–6969

Geim AK (2009) Graphene: status and prospects. Science 324:1530–1534

Gowri S, Gandhi RR, Sundrarajan M (2014) Structural, optical, antibacterial and antifungal properties of zirconia nanoparticles by biobased protocol. J Mater Sci Technol 30:782–790

Guo S, Dong S (2011) Graphene nanosheet: synthesis, molecular engineering, thin film, hybrids, and energy and analytical applications. Chem Soc Rev 40:2644–2672

He Y, Cai J, Li T, Wu Y, Lin H, Zhao L, Luo M (2013) Efficient degradation of RhB over $GdVO_4$/g-C_3N_4 composites under visible-light irradiation. Chem Eng J 215:721–730

Hu R, Wang X, Dai S, Shao D, Hayat T, Alsaedi A (2015) Application of graphitic carbon nitride for the removal of Pb(II) and aniline from aqueous solutions. Chem Eng J 260:469–477

Huang Z-F et al (2015) Carbon nitride with simultaneous porous network and O-doping for efficient solar-energy-driven hydrogen evolution. Nano Energy 12:646–656

Jiang H, Gomez-Abal RI, Rinke P, Scheffler M (2010) Electronic band structure of zirconia and hafnia polymorphs from the G W perspective. Phys Rev B 81:085119

Jiang F, Yan T, Chen H, Sun A, Xu C, Wang X (2014) A g-C_3N_4–CdS composite catalyst with high visible-light-driven catalytic activity and photostability for methylene blue degradation. Appl Surf Sci 295:164–172

Klibanov AM, Tu T-M, Scott KP (1983) Peroxidase-catalyzed removal of phenols from coal-conversion waste waters. Science 221:259–261

Lan M, Fan G, Yang L, Li F (2015) Enhanced visible-light-induced photocatalytic performance of a novel ternary semiconductor coupling system based on hybrid Zn–In mixed metal oxide/g-C_3N_4 composites. RSC Adv 5:5725–5734

Leary R, Westwood A (2011) Carbonaceous nanomaterials for the enhancement of TiO_2 photocatalysis. Carbon 49:741–772

Li G, Wong K, Zhang X, Hu C, Jimmy CY, Chan R, Wong P (2009) Degradation of acid orange 7 using magnetic AgBr under visible light: the roles of oxidizing species. Chemosphere 76:1185–1191

Li G et al (2015) Enhanced visible-light-driven photocatalytic inactivation of *Escherichia coli* using g-C_3N_4/TiO_2 hybrid photocatalyst synthesized using a hydrothermal-calcination approach. Water Res 86:17–24

Liang Q, Li Z, Yu X, Huang ZH, Kang F, Yang QH (2015) Macroscopic 3D porous graphitic carbon nitride monolith for enhanced photocatalytic hydrogen evolution. Adv Mater 27:4634–4639

Liu G, Wang Y, Shen C, Ju Z, Yuan D (2015a) A facile synthesis of microporous organic polymers for efficient gas storage and separation. J Mater Chem A 3(6):3051–3058

Liu J et al (2015b) Metal-free efficient photocatalyst for stable visible water splitting via a two-electron pathway. Science 347:970–974

Lu Y-C, Chen J, Wang A-J, Bao N, Feng J-J, Wang W, Shao L (2015) Facile synthesis of oxygen and sulfur co-doped graphitic carbon nitride fluorescent quantum dots and their application for mercury (II) detection and bioimaging. J Mater Chem C 3:73–78

Luo WB, Chou SL, Wang JZ, Zhai YC, Liu HK (2015) A metal-free, free-standing, macroporous graphene@ g-C_3N_4 composite air electrode for high-energy lithium oxygen batteries. Small 11:2817–2824

Maeda K, Kuriki R, Zhang M, Wang X, Ishitani O (2014) The effect of the pore-wall structure of carbon nitride on photocatalytic CO_2 reduction under visible light. J Mater Chem A 2:15146–15151

Mao J, Peng T, Zhang X, Li K, Ye L, Zan L (2013) Effect of graphitic carbon nitride microstructures on the activity and selectivity of photocatalytic CO_2 reduction under visible light. Catal Sci Technol 3:1253–1260

Ong W-J, Tan L-L, Chai S-P, Yong S-T (2015a) Graphene oxide as a structure-directing agent for the two-dimensional interface engineering of sandwich-like graphene–gC_3N_4 hybrid nanostructures with enhanced visible-light photoreduction of CO_2 to methane. Chem Commun 51:858–861

Ong W-J, Tan L-L, Chai S-P, Yong S-T (2015b) Heterojunction engineering of graphitic carbon nitride (gC_3N_4) via Pt loading with improved daylight-induced photocatalytic reduction of carbon dioxide to methane. Dalton Trans 44:1249–1257

Pany S, Parida K (2015) A facile in situ approach to fabricate N, S-TiO_2/g-C_3N_4 nanocomposite with excellent activity for visible light induced water splitting for hydrogen evolution. Phys Chem Chem Phys 17:8070–8077

Papailias I, Giannakopoulou T, Todorova N, Demotikali D, Vaimakis T, Trapalis C (2015) Effect of processing temperature on structure and photocatalytic properties of g-C_3N_4. Appl Surf Sci 358:278–286

Pawar RC, Kang S, Ahn SH, Lee CS (2015) Gold nanoparticle modified graphitic carbon nitride/multi-walled carbon nanotube (g-C_3N_4/CNTs/Au) hybrid photocatalysts for effective water splitting and degradation. RSC Adv 5:24281–24292

Pawar RC, Kang S, Park JH, Kim J-H, Ahn S, Lee CS (2016a) Room-temperature synthesis of nanoporous 1D microrods of graphitic carbon nitride (g-C_3N_4) with highly enhanced photocatalytic activity and stability. Sci Rep 6:31147

Pawar RC, Son Y, Kim J, Ahn SH, Lee CS (2016b) Integration of ZnO with g-C_3N_4 structures in core–shell approach via sintering process for rapid detoxification of water under visible irradiation. Curr Appl Phys 16:101–108

Pawar RC, Kang S, Park JH, Kim J-H, Ahn S, Lee CS (2017) Evaluation of a multi-dimensional hybrid photocatalyst for enrichment of H 2 evolution and elimination of dye/non-dye pollutants. Catal Sci Technol 7:2579–2590

Pohanish RP (2008) Sittig's handbook of toxic and hazardous chemicals and carcinogens. William Andrew, Norwich

Polisetti S, Deshpande PA, Madras G (2011) Photocatalytic activity of combustion synthesized ZrO2 and ZrO2–TiO2 mixed oxides. Ind Eng Chem Res 50:12915–12924

Pradhan N, Pal A, Pal T (2002) Silver nanoparticle catalyzed reduction of aromatic nitro compounds. Colloids Surf A 196:247–257

Reimer T et al (2014) Single step integration of ZnO nano-and microneedles in Si trenches by novel flame transport approach: whispering gallery modes and photocatalytic properties. ACS Appl Mater Interfaces 6:7806–7815

Sayama K, Arakawa H (1993) Photocatalytic decomposition of water and photocatalytic reduction of carbon dioxide over zirconia catalyst. J Phys Chem 97:531–533

Singh A, Nakate UT (2014) Microwave synthesis, characterization, and photoluminescence properties of nanocrystalline zirconia. Sci World J Article ID 349457:1–7

Song C, Zhang J (2008) Electrocatalytic oxygen reduction reaction. In: PEM fuel cell electrocatalysts and catalyst layers. Springer, pp 89–134

Sridharan K, Kuriakose T, Philip R, Park TJ (2014) Transition metal (Fe, Co and Ni) oxide nanoparticles grafted graphitic carbon nitrides as efficient optical limiters and recyclable photocatalysts. Appl Surf Sci 308:139–147

Tan L-L, Ong W-J, Chai S-P, Goh BT, Mohamed AR (2015) Visible-light-active oxygen-rich TiO_2 decorated 2D graphene oxide with enhanced photocatalytic activity toward carbon dioxide reduction. Appl Catal B Environ 179:160–170

Tian J, Liu Q, Asiri AM, Al-Youbi AO, Sun X (2013) Ultrathin graphitic carbon nitride nanosheet: a highly efficient fluorosensor for rapid, ultrasensitive detection of Cu^{2+}. Anal Chem 85:5595–5599

Tian J, Ning R, Liu Q, Asiri AM, Al-Youbi AO, Sun X (2014) Three-dimensional porous supramolecular architecture from ultrathin g-C_3N_4 nanosheets and reduced graphene oxide: solution self-assembly construction and application as a highly efficient metal-free electrocatalyst for oxygen reduction reaction. ACS Appl Mater Interfaces 6:1011–1017

Wang D, Astruc D (2014) Fast-growing field of magnetically recyclable nanocatalysts. Chem Rev 114:6949–6985

Wang X et al (2009) A metal-free polymeric photocatalyst for hydrogen production from water under visible light. Nat Mater 8:76–80

Wang Y, Wang X, Antonietti M (2012) Polymeric graphitic carbon nitride as a heterogeneous organocatalyst: from photochemistry to multipurpose catalysis to sustainable chemistry. Angew Chem Int Ed 51:68–89

Wang H, Lu J, Wang F, Wei W, Chang Y, Dong S (2014) Preparation, characterization and photocatalytic performance of g-C_3N_4/Bi_2WO_6 composites for methyl orange degradation. Ceram Int 40:9077–9086

Wang L, Zhao F, Han Q, Hu C, Lv L, Chen N, Qu L (2015) Spontaneous formation of Cu_2O–g-C_3N_4 core–shell nanowires for photocurrent and humidity responses. Nanoscale 7:9694–9702

Woan K, Pyrgiotakis G, Sigmund W (2009) Photocatalytic carbon-nanotube–TiO_2 composites. Adv Mater 21:2233–2239

Wu Z, Gao H, Yan S, Zou Z (2014) Synthesis of carbon black/carbon nitride intercalation compound composite for efficient hydrogen production. Dalton Trans 43:12013–12017

Xu H, Ouyang S, Liu L, Reunchan P, Umezawa N, Ye J (2014) Recent advances in TiO_2-based photocatalysis. J Mater Chem A 2:12642–12661

Xu L et al (2015) Insights into enhanced visible-light photocatalytic hydrogen evolution of g-C3N4 and highly reduced graphene oxide composite: the role of oxygen. Chem Mater 27:1612–1621

Yan S, Li Z, Zou Z (2009) Photodegradation performance of g-C_3N_4 fabricated by directly heating melamine. Langmuir 25:10397–10401

Yan S, Lv S, Li Z, Zou Z (2010) Organic–inorganic composite photocatalyst of g-C_3N_4 and TaON with improved visible light photocatalytic activities. Dalton Trans 39:1488–1491

Yang X, Cui H, Li Y, Qin J, Zhang R, Tang H (2013) Fabrication of Ag_3PO_4-graphene composites with highly efficient and stable visible light photocatalytic performance. ACS Catal 3:363–369

Yang J, Zhang H, Chen B, Tang H, Li C, Zhang Z (2015a) Fabrication of the gC_3N_4/Cu nanocomposite and its potential for lubrication applications. RSC Adv 5:64254–64260

Yang Q, Wang W, Zhao Y, Zhu J, Zhu Y, Wang L (2015b) Metal-free mesoporous carbon nitride catalyze the Friedel–Crafts reaction by activation of benzene. RSC Adv 5:54978–54984

Yeh T-F, Chen S-J, Teng H (2015) Synergistic effect of oxygen and nitrogen functionalities for graphene-based quantum dots used in photocatalytic H_2 production from water decomposition. Nano Energy 12:476–485

Yi J, Liao K, Zhang C, Zhang T, Li F, Zhou H (2015) Facile in situ preparation of graphitic-C_3N_4@ carbon paper as an efficient metal-free cathode for nonaqueous Li–O_2 battery. ACS Appl Mater Interfaces 7:10823–10827

Zarei M, Seif A, Azizi K, Zarei M, Bahrami J (2016) Effect of phenolic radicals on the geometry and electronic structure of DNA base pairs: computational study. Int J Mod Phys C 27:1650119

Zhang X, Zhang L, Xie T, Wang D (2009) Low-temperature synthesis and high visible-light-induced photocatalytic activity of BiOI/TiO_2 heterostructures. J Phys Chem C 113:7371–7378

Zhang Q, Zhang Y, Li H, Gao C, Zhao Y (2013) Heterogeneous CaO-ZrO_2 acid–base bifunctional catalysts for vapor-phase selective dehydration of 1, 4-butanediol to 3-buten-1-ol. Appl Catal A Gen 466:233–239

Zhang H et al (2015a) Self-assembly of graphitic carbon nitride nanosheets–carbon nanotube composite for electrochemical simultaneous determination of catechol and hydroquinone. Electrochim Acta 176:28–35

Zhang P, Wang T, Gong J (2015b) Mechanistic understanding of the plasmonic enhancement for solar water splitting. Adv Mater 27:5328–5342

Zhao Y, Zhang Y, Li J, Du X (2014) Solvothermal synthesis of visible-light-active N-modified ZrO_2 nanoparticles. Mater Lett 130:139–142

Zhao L et al (2015) A chromium nitride/carbon nitride containing graphitic carbon nanocapsule hybrid as a Pt-free electrocatalyst for oxygen reduction. Chem Commun 51:12399–12402

Zheng Y, Liu J, Liang J, Jaroniec M, Qiao SZ (2012) Graphitic carbon nitride materials: controllable synthesis and applications in fuel cells and photocatalysis. Energy and Environ Sci 5:6717–6731